Research Square

Preprints are preliminary reports that have not undergone peer review.
They should not be considered conclusive, used to inform clinical practice,
or referenced by the media as validated information.

High Gain Non-Isolated Switched Inductor SEPIC Converter for Renewable Energy Applications

Dileep. Gopalakrishnan

Dileep.Gopalakrishnan.1@uni.massey.ac.nz

Massey University

Arunkumar C R

Visteon (United States)

Vishnu Sidharthan

National Institute of Technology Karnataka

Sreekanth Nethagani

Royal Government of Bhutan

Article

Keywords: PSO, MPPT, PSCs, PV generation system, SEPIC

Posted Date: August 12th, 2026

DOI: https://doi.org/10.21203/rs.3.rs-10419105/v1

License: This work is licensed under a Creative Commons Attribution 4.0 International License.
Read Full License

Additional Declarations: No competing interests reported.

Version of Record: A version of this preprint was published at Scientific Reports on November 3rd, 2026.
See the published version at https://doi.org/10.1038/s41598-026-76697-1.

High Gain Non-Isolated Switched Inductor SEPIC Converter for Renewable Energy Applications

[1]Dileep. Gopalakrishnan, [2]Arunkumar C R, [3]Vishnu Sidharthan P, [4]Sreekanth Nethagani,

[1]College of Creative Arts, Massey University, Wellington, New Zealand
[1]Visteon Portuguesa, Palmela, Portugal
[3]National Institute of Technology, Surathkal, Karnataka, India
[4]Jigme Namgyel Engineering College, Royal University of Bhutan, Dewathang, Bhutan
* Corresponding author: Dileep. Gopalakrishnan (e-mail: Dileep.Gopalakrishnan.1@uni.massey.ac.nz)

Abstract

High step-up DC-DC converters are required in renewable energy systems to efficiently interface low-voltage sources with high-voltage loads and DC microgrids. The conventional high gain converter suffers from high voltage stress of semiconductor devices, low efficiency and complex circuit architecture. A high gain non-isolated switched inductor single-ended primary-inductor converter (SI-SEPIC) for renewable energy applications is presented in this research. The suggested topology adopts the switched-inductor network to realize a much higher voltage conversion ratio. The converter retains the intrinsic benefits of standard SEPIC converter, such as non-inverted output voltage and wide working range, which make it suited for solar systems, fuel cells, battery-powered systems and DC microgrids. The converter is analyzed in detail in terms of operating modes, steady state characteristics, derivation of voltage gain, design of components and performance evaluation. The proposed converter is experimentally validated with a laboratory prototype of 75 W. The experimental results support the validity of the proposed SI-SEPIC converter for renewable energy applications with steady operation; high voltage gain and high-power conversion efficiency.

Keywords: PSO, MPPT, PSCs, PV generation system, SEPIC.

Introduction

The study of other energy resources, like solar, hydro, wind, and fuel cells, has been encouraged by the increased energy demand globally and rising environmental concerns. Due to their cleanliness, abundance, and boundless supply, SPV systems have gathered a lot of attention amongst renewable energy sources. Though, photovoltaics depends on changing solar irradiation all over the day, the power it generates is inherently unpredictable. One of the most significant components of SPV systems is the MPPT. The peak power production of an SPV module, together with its operating current and voltage, varies with fluctuations in solar insolation and temperature. To take full advantage of energy extraction, an SPV module should be driven at the voltage connected to its MPP. To capture the varying maximum power, SPV systems employ a DC–DC

converter combined with a MPPT module. These converter act as impedance-matching circuit, efficiently connecting the PV panel to the load. By fine-tuning the converter duty cycle, its input impedance can be tuned to the PV panel output impedance, thereby accomplishing effective load matching. Numerous MPPT techniques have been established to achieve this task. Normally employed MPPT techniques include current and voltage-based techniques, as well as traditional algorithms like perturb and observe (P&O) [1] and incremental conductance (INC) [2]. Furthermore, intelligent control methods, like fuzzy logic control (FLC) and artificial neural networks (ANN) [3], are employed frequently. Voltage and current derived MPPT techniques are forthright to establish but usually suffer from low efficiency and accuracy. The short-circuit current scheme [4] needs only a solitary sensor and is modest in design; though, it requires brief short-circuiting the SPV module through a switch to estimate the short-circuit current (Isc). The open-circuit voltage (Voc) technique [5] illustrates another simple MPPT method; though, it needs periodic measurement of Voc, which is attained by momentarily disabling the converter. This method, though, presents a few drawbacks, including a momentary power loss throughout measurement. To alleviate this issue, pilot cells can be used to find the Voc. These pilot cells should be selected wisely to make sure that their electrical features replicate closely those of the key PV array. Under short-circuit and open-circuit circumstances, the SPV module carries no power to the load, thus dropping overall efficiency. Ripple correlation control (RCC) [6] tackles some of the drawbacks linked with the P&O technique. Sliding mode control (SMC) [7] offers more accurate tracking of the MPP compared to traditional approaches, even though its hardware enactment is reasonably complex. Temperature-based MPPT methods [8] need less sensors, making them inexpensive and forthright to implement. The bisection search theorem technique [9] can be employed to track the MPP of PV modules that display numerous local maxima under fluctuating climatic conditions. Moreover, a dual MPPT tracking scheme has been discussed in [10]. Mechanical tracking structures orient the PV module physically in the direction of maximum sunlight, while electrical tracking can be achieved using an MPPT algorithm. ANN-based MPPT practices [11], [12] estimate the reference voltage by seeing solar irradiation and cell temperature. Unlike traditional methods, ANN does not need complete system data to accomplish effective tracking. The neuro-fuzzy method [13] incorporates the advantages of both fuzzy controllers and neural network. In this technique, the neural network estimates the optimum operating voltage, while the FLC is utilized to adjust the duty ratio of the converter appropriately. System oscillation control derived MPPT methods [14], [15] needs only a single voltage sensor, making them modest to realize and free from complex mathematical computations. State space derived MPPT [16] converts the time-varying, nonlinear SPV system into a linear dynamic model, thus enabling easier tracking of the MPP. Linearization-based MPPT [17] is a fast, modest, and economical method. This technique also converts the nonlinear current and power formulas into linear forms, thus facilitating MPP tracking. The array reconfiguration technique [18], on the other hand, is a mechanical technique in which PV arrays are reorganized into parallel or series combinations to reach the MPP. Numerical analysis based MPPT [19] determines the voltage at the MPP using a quadratic interpolation technique. This algorithm computes the precise voltage value

mathematically, permitting the MPP to be reached in one step; but the technique is computationally complex. PSO based MPPT determines peak power effectively under changing atmospheric conditions.

Selecting a suitable DC–DC converter for PV power tracking applications comprises of evaluating efficiency, PV module interaction, cost, energy transfer characteristics, and operational flexibility. Broadly used converter categories comprise of Boost, Buck, Buck–Boost, SEPIC, and Ćuk converters. Boost converters [20], [21] are used extensively for voltage step-up applications, offering constant energy transfer and high efficiency at low cost. However, their incapability to reduce voltage limits flexibility and can deter precise MPP tracking in some scenarios. The Buck converter [22] is employed for the voltage step down and its power flow is not steady since the input-side switch operates continuously, temporarily isolating the PV array from the load. Moreover, the Buck converter lacks the capability to step up the voltage, which can affect tracking peak power adversely under some operating conditions. Buck–Boost, Ćuk, and SEPIC network topologies are proficient of performing both step-up and step-down operations. Alike to the Buck converter, the power flow of the Buck–Boost converter [23] is discontinuous in nature, and the incessant operation of the input-side switch leads in higher switching losses. The Buck–Boost converter provides flexible maximum power point tracking by allowing both step-up and step-down functionalities; though, its output voltage is inverted. The Ćuk converter [24] accomplishes higher efficiency than the Buck–Boost topology and sustains unremitting input/output power flow, however its output voltage is also inverted. Conversely, the SEPIC converter [25], [26] offers non-inverted output voltage together with continuous energy transfer and enhanced efficiency, making it more appropriate for photovoltaic applications. Owing to these intrinsic advantages, the SEPIC converter is chosen over other converters for this work.

This paper proposes an enhanced MPPT algorithm combined with an improved SEPIC converter. The conventional PSO technique is modified to serve as the MPPT algorithm for tracking the Global MPP (GMPP) under PSCs. The proposed technique is verified by realizing experimental set up in the laboratory, where a SEPIC converter is fed by a solar array simulator, and the control action is implemented via an OPAL-RT microcontroller.

Working principle of the SI-SEPIC converter

As depicted in Figure 1, SI structures are used in place of the input and output side inductors of the traditional SEPIC converter to boost gain. When the switch is ON, every inductor charges simultaneously, and when the switch is OFF, every inductor discharges simultaneously. The proposed converter operates in a symmetrical manner on two half-line cycles of the input voltage. Consequently, this section explains the converter's operation during a single transition period in positive half-line cycles of the input voltage. The converter is presumed to be in continuous conduction mode (CCM). It is assumed that the converter is in a stable condition and that every component of the circuit is perfect. It is expected that the output capacitor, C_o, is adequately big to lessen the output voltage ripple.

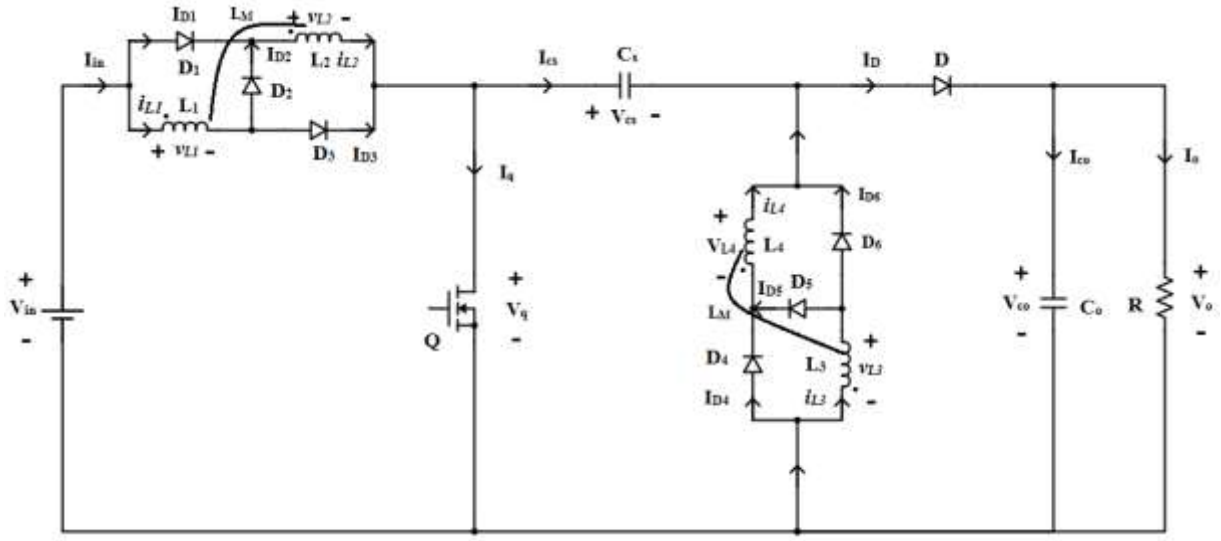


Fig. 1. Circuit diagram of SI- SEPIC converter.

Mode: 1 *(0 < t <DT):* Prior to this mode, the inductor currents i_{L1}, i_{L2}, i_{L3} *and* i_{L4} are minimum and voltage across the coupling capacitor, V_{cs} is maximum, which is equal to input voltage V_{in}. When switch Q is activated, Mode 1 begins, diodes D_1, D_3, D_4, and D_6, are forward biased whereas diodes D_2, D_5, and D are reverse biased. V_{in} starts charging inductors L_1 and L_2 in parallel with linearly increasing currents , i_{L1} *and* i_{L2} with slopes $\frac{V_{in}}{L_1}$ and $\frac{V_{in}}{L_2}$ respectively. The supply voltage, V_{in} equals to the voltage across the inductors L_1 and L_2. In this phase, the coupling capacitor's energy is transmitted via the switch to inductors L_3 and L_4. Inductor currents i_{L3} *and* i_{L4} increases linearly with a slope $\frac{V_{cs}}{L_3}$ and $\frac{V_{cs}}{L_4}$ respectively. Since diode, D, is reverse biased input is completely isolated from the output, and capacitor C_o keeps the load current uninterrupted. Figure 2 depicts the equivalent circuit of the SI-SEPIC converter during Mode 1.

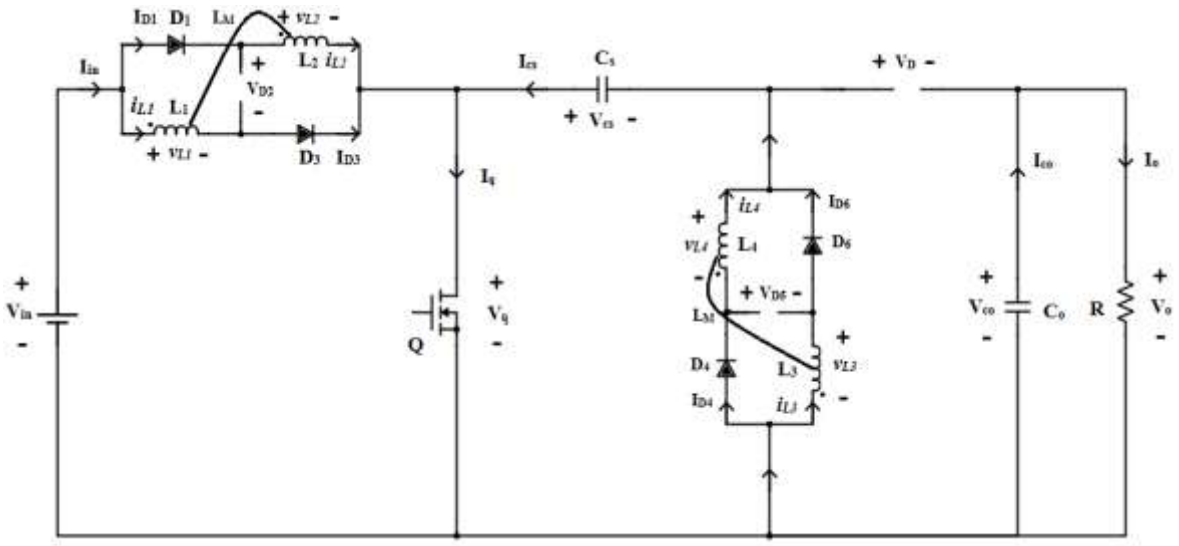


Fig. 2. Equivalent circuit when the switch is turned ON in Mode 1.

Applying KVL in source side considering, L_1,

$$v_{L1} = V_{in} = L_1 \frac{di_{L1}}{dt} \tag{1}$$

From Eq. (1) ripple current through inductor L_1,

$$(\Delta i_{L1})_{closed} = \frac{V_{in} DT}{L_1} \tag{2}$$

Similarly, ripple current through inductor L_2,

$$(\Delta i_{L2})_{closed} = \frac{V_{in} DT}{L_2} \tag{3}$$

Applying KVL in coupling capacitor side by considering, L_3,

$$v_{L3} = V_{cs} = L_3 \frac{di_{L3}}{dt} \tag{4}$$

From Eq. (4) ripple current through inductor L_3,

$$(\Delta i_{L3})_{closed} = \frac{V_{cs} DT}{L_3} \tag{5}$$

Similarly, ripple current through inductor L_2,

$$(\Delta i_{L4})_{closed} = \frac{V_{cs} DT}{L_4} \tag{6}$$

Voltage across the coupling capacitor C_s is,

$$V_{cs} = V_{in} \tag{7}$$

Comparing Eqs. (2), (3), (5), (6) and (7),

$$(\Delta i_{L1})_{closed} = (\Delta i_{L2})_{closed} = (\Delta i_{L3})_{closed} = (\Delta i_{L4})_{closed} = \frac{V_{in} DT}{L} \tag{8}$$

were, $L_1 = L_2 = L_3 = L_4 = L$,

Mode: 2 *(DT < t <T):* Before entering this mode, inductor currents $i_{L1}, i_{L2}, i_{L3} and\ i_{L4}$ is maximum and V_{cs} is minimum. When the switch is turned off, mode 2 begins, diodes D_2, D_5, and

D are forward biased whereas diodes D_1, D_3, D_4, and D_6, are reverse biased. The coupling capacitor receives the energy from the inductors L_1 and L_2. Via diode D, energy from inductors L_3 and L_4 as well as V_{in} is transmitted to the load. This is the time when the output capacitor C_o is fully charged. With a slope of $\frac{V_o}{2L_1}$, $\frac{V_o}{2L_2}$, $\frac{V_o}{2L_3}$ and $\frac{V_o}{2L_4}$ respectively, inductor currents i_{L1}, i_{L2}, i_{L3} and i_{L4}, decreases linearly. During this time, the voltage across inductors equals $\frac{V_o}{2}$. Figure 3 depicts the equivalent circuit of the SI-SEPIC converter during Mode 2.

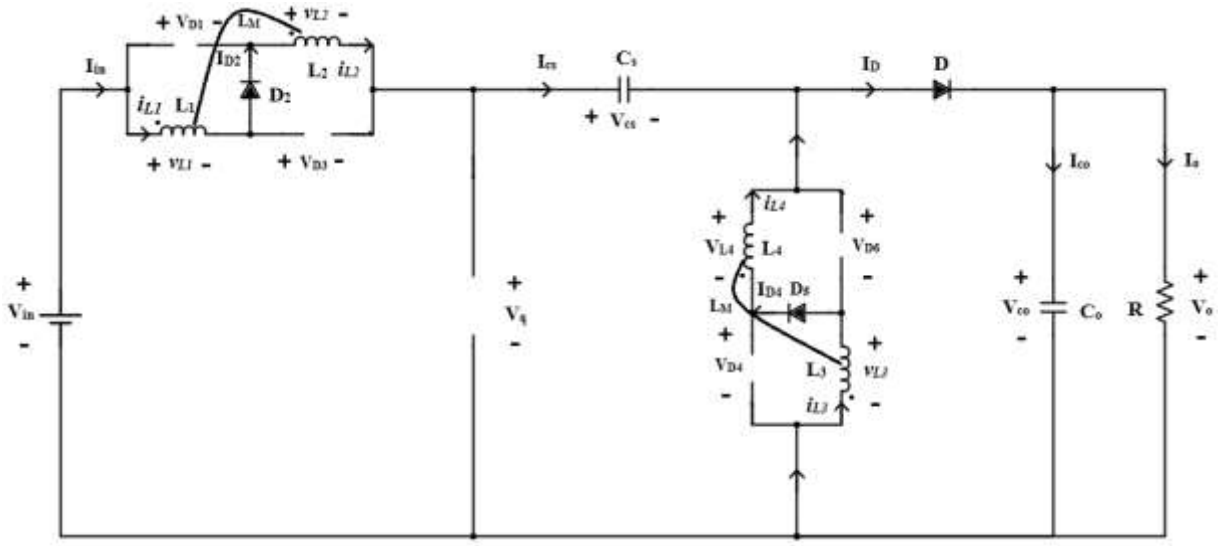


Fig. 3. Equivalent circuit when the switch is turned OFF in Mode 2.

Applying KVL in source side, ripple current through inductor L_1,

$$(\Delta i_{L1})_{open} = \frac{V_{in} - V_{cs} - V_o - v_{L2}}{L_1}(1-D)T \tag{9}$$

Similarly, ripple current through inductor L_2,

$$(\Delta i_{L2})_{open} = \frac{V_{in} - V_{cs} - v_{L1}}{L_2}(1-D)T \tag{10}$$

Applying KVL in output loop, ripple current through inductor L_3,

$$(\Delta i_{L3})_{closed} = \frac{V_o - v_{L4}}{L_3}(1-D)T \tag{11}$$

Similarly, ripple current through inductor L_2,

$$(\Delta i_{L4})_{closed} = \frac{V_o - v_{L3}}{L_4}(1-D)T \tag{12}$$

Since all the inductors have same the value voltage across inductors are,

$$v_{L1} = v_{L2} = v_{L3} = v_{L4} = \frac{V_o}{2} \tag{13}$$

Comparing Eqs. (9), (10), (11), (12) and (13),

$$(\Delta i_{L1})_{closed} = (\Delta i_{L2})_{closed} = (\Delta i_{L3})_{closed} = (\Delta i_{L4})_{closed} = \frac{V_o(1-D)T}{2L} \tag{14}$$

DC Voltage transfer function

Applying volt-sec balance theorem, and combining Equations (8) and (14),

$$\frac{V_{in}DT}{L_1} + \frac{V_{in} - V_{cs} - v_{L2}}{L_1}(1-D)T = 0 \quad (15)$$

Since L_1=L_2=L_3=L_4 ,voltage across inductor L_1 and L_2 when switch is closed will be, combining Eqs. (7), (13) and (15),

$$\frac{V_{in}DT}{L} - \frac{V_o}{2L}(1-D)T = 0 \quad (16)$$

From Eq. (16) DC voltage transfer function, M_{vdc} for the proposed converter can be derived as,

$$M_{vdc} = \frac{V_o}{V_{in}} == \frac{2D}{1-D} \quad (17)$$

Design Methodology of the SI-SEPIC Converter

The proposed converter's design process is alike to that of a traditional SEPIC converter. This section explains the SI-SEPIC converter design process for a PV module with the following specifications:

Minimum input voltage, $V_{in(min)} = 4$ V

Maximum input voltage, $V_{in(max)} = 21$ V

Output voltage, $V_o = 24$ V

Switching frequency, $f_S = 50$ kHz

Duty cycle analysis

Eqs. (18) and (19) provide the maximum and minimum duty cycle values for a SI-SEPIC converter running in continuous conduction mode (CCM);

$$\alpha_{\max} = \frac{V_o}{2V_{in(\min)} + V_o} = 0.75 \quad (18)$$

And,

$$\alpha_{\min} = \frac{V_o}{2V_{in(\max)} + V_o} = 0.36 \quad (19)$$

Selection of Inductors

The maximum input current is around 20% of the inductor's peak-to-peak ripple current. The ripple currents flowing through the inductors are given by,

$$\Delta I_L = I_{in} \times 20\% \quad (20)$$

Substituting for I_{in},

$$\Delta I_L = I_o \times \frac{V_o}{V_{in(min)}} \times 20\% = 3.75\text{A} \quad (21)$$

And the inductance L_1, L_2, L_3 and L_4 are obtained as,

$$L_1 = L_2 = L_3 = L_4 = \frac{V_{in(min)}}{\Delta I_L \times f_{sw}} \times \alpha_{\max} = 16\mu H \quad (22)$$

Selection of Output Capacitor

RMS current of output capacitor,

$$I_{co(rms)} = I_o \sqrt{\frac{V_o(V_{in} + 2V_o)}{V_{in}(2V_{in} + V_o)}} = 3.27A \tag{23}$$

Assuming that the output voltage's peak-to-peak ripple is 2%, the ESR of output capacitor's is,

$$ESR \le \frac{\Delta V_o \times 0.5}{2I_{L1(peak)} + 2I_{L3(peak)}} = 26m\Omega \tag{24}$$

The RMS current is used to choose the coupling capacitor. This makes SI-SEPIC converter more suitable for low power application, where the RMS current is relatively very small. The output capacitance is,

$$C_o \ge \frac{I_o \times \alpha_{\max}}{\Delta V_o \times 0.5 \times f_{sw}} = 195.31\mu F \tag{25}$$

Coupling capacitor selection

Coupling capacitor RMS current is,

$$I_{cs(rms)} = I_o \sqrt{\frac{V_o(V_{in} + 2V_o)}{V_{in}(2V_{in} + V_o)}} = 3.27A \tag{26}$$

Assuming peak to peak ripple 2% of the output voltage, the output capacitor is,

$$C_s \ge \frac{I_o \times \alpha_{\max}}{\Delta V_o \times f_{sw}} = 97.66\mu F \tag{27}$$

Selection Power MOSFET

Peak current through the MOSFET is given by,

$$I_{q(peak)} = 2I_{L1(peak)} + 2I_{L3(peak)} = 7.625A \tag{28}$$

RMS current the MOSFET switch,

$$I_{q(rms)} = \frac{I_o}{2} \sqrt{\frac{V_o(2V_{in} + V_o)}{V_{in}^{\ 2}}} = 2.96A \tag{29}$$

Diode selection

The average diode current equals the output current, and the rated reverse current of the output diode must be higher than $V_{in}+V_O$. The rated reverse current of diodes in switched inductor structure is V_{in} during ON period and $V_O/2$ during OFF period and the average current through these diodes are equal to average inductor currents.

Development of MPPT algorithm

In this article, the MPPT algorithm for PV systems is implemented using an enhanced PSO approach. The variable of choice is the converter's duty cycle. The duty cycle as the regulated variable eliminates proportional integral controller which is required for voltage-based controllers.

Outline of Conventional PSO algorithm

A population-based swarm intelligence method called PSO was first presented by Kennedy and Eberhart in 1995 with the goal of resolving engineering optimization issues with local optima [27]. PSO is employed to find the optimal solution in an n-dimensional search space for a given optimization problem and is motivated by the social behavior seen in fish schools and bird flocks [28]. To discover the best solution, a population of particles, also referred to as cooperative agents is employed. In order to identify the best solution, every particle (or agent) in the population adheres to two basic rules: it monitors the top-performing particle and the optimum solution discovered on its own. As a result, every particle in the population moves closer to the optimal solution. Using Eq. (30), particle locations within a population are modified [29],

$$x_i^{k+1} = x_i^k + \emptyset_i^{k+1} \tag{30}$$

where the velocity component, denoted by $\emptyset_i$, is computed using Eq. (31),

$$\emptyset_i^{k+1} = \omega \times \emptyset_i + c_1 \times r_1 \times \left\{P_{besti} - x_i^k\right\} + c_2 \times r_2 \times \{G_{best} - x_i^k\} \tag{31}$$

where ω represents the inertia weight, r_1 and r_2 are random variables scattered uniformly inside [0, 1], c_1 and c_2 represents the cognitive coefficient and social coefficients, P_{besti} represents the optimal position of ith particle and G_{best} represents optimal position of all particles.

Step 1 (Setting up PSO): The number of particles is specified, and they are evenly dispersed across the optimization problem's n-dimensional space. The beginning velocity is selected at random, and the cognitive coefficient, social coefficient, and inertia weight are defined.

Step 2 (Assessment of the fitness function): For every particle, the fitness function that has to be optimized is assessed. By replacing the objective function with the candidate solution, the fitness function is evaluated.

Step 3 (Updating individual and global best): If the current fitness value is higher than the individual and global optimal values, the fitness value relating to the particle's current location is modified.

Step 4 (Upadating position and velocity of particles): Eq. (30) and Eq. (31) are used to modify the location and velocity of each particle.

Step 5 (Looking for convergence): If the convergence conditions are satisfied, the procedure ends; if not, the number of iterations is raised by one, and step 2 is reached.

Enhancing and using PSO in MPPT

An MPPT controller for an SPV system is implemented using the PSO algorithm described in Section 3.1, allowing for efficient peak power tracking under PSCs. The traditional PSO approach is further enhanced to improve tracking accuracy, speed, and durability. There are a number of hybrid [30-33] and improved [34-44] PSO MPPT techniques. By raising the social coefficient from lower to higher values and linearly lowering the cognitive coefficient and inertia weight from higher to lower values. The inertial weight, ω controls the agents' inertia. Convergence accelerates if ω is too big, yet overshooting may result. On the other hand, if it is too tiny, the agents can alter their direction of motion more readily, but convergence slows down. Consequently, convergence speed, tracking accuracy, and agent movement behavior inside the search space are all improved by progressively lowering ω from a higher beginning value to a lower value over repetitions. c_1 Without assistance from other agents, c_1 identifies each agent's unique search capacity. The agents may prematurely converge to local maxima if c_1 is very big. On the other hand, if it is too small, agents' convergence toward the ideal operating point slows down. To guarantee that the agents converge toward G_{best} in the least amount of time, c_1 is also adjusted from a comparatively larger value to a lower one, much like ω. c_2 controls the agents' capacity for cooperative search. The agents prefer to converge at separate sites if it is small, which causes the convergence pace to be sluggish. On the other hand, if it is big, the agents are more likely to converge close to the MPP and the search space becomes constrained. Over the course of several rounds, c_2 is progressively raised from a comparatively lower number to a higher value in order to precisely and accurately monitor G_{best} in the least amount of time. Increasing the number of agents makes it possible to identify the MPP under different atmospheric circumstances, but this increases the total convergence time. Achieving quick convergence in the shortest tracking time is a major problem in MPPT applications. In order to meet the realistic criteria of the MPP issue, the basic APSO method is changed. Figure 4 displays the block diagram for the suggested system. A Chroma 62150H-600S solar array simulator running in SAS mode is linked to the load via a SEPIC converter, as shown in Figure 5, and the MPPT algorithm is implemented using an OPAL-RT OP5600 controller.

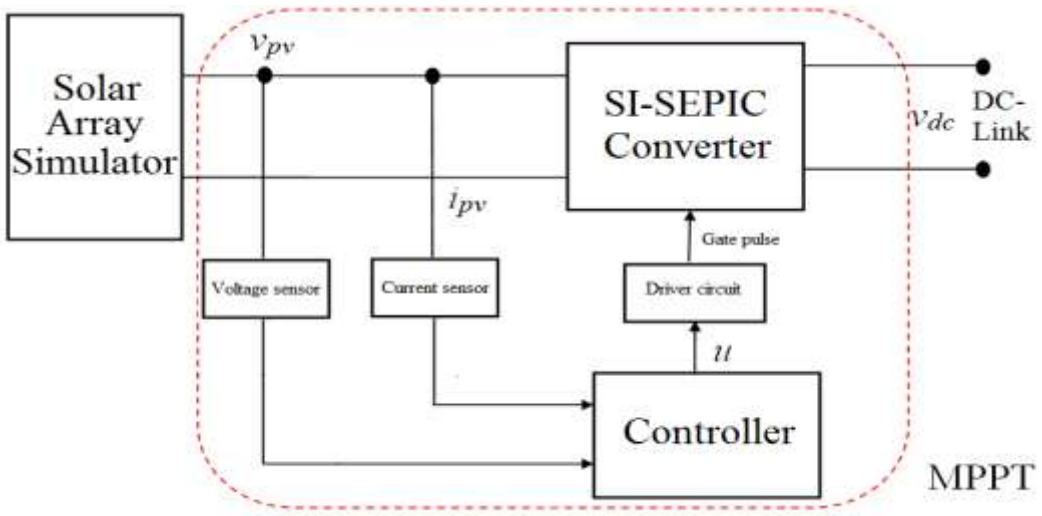


Fig. 4. Block schematic of the suggested system.

The following is a description of the working principles of the suggested APSO-based MPPT technique:

Step 1 (Selection of system parameters): The particle location is determined by the DC–DC converter's duty ratio (D). The objective function to be maximized is the power drawn from the PV panel P_{PV}. A bigger population increases tracking accuracy but decreases tracking speed, hence the number of particles in the population is carefully chosen. Furthermore, the calculation time increases as the number of particles increases. In order to attain an appropriate trade-off between tracking accuracy and speed, the population size is selected. The number of PV cells connected in series is often used to calculate the population size.

Step 2 (Setting up APSO): Particles from the chosen population may be randomly scattered across the search space or initiated at predetermined locations in APSO. The particles can be initiated in the area of the GMPP if previous knowledge about it is available. A PV characteristic's MPP usually happens at around 80% of the open-circuit voltage. As a result, inside the search space defined by the maximum and minimum bounds, D_{max} and D_{min}, respectively, the particles are typically started at fixed, evenly spaced places.

Step 3 (Assessment of the fitness function): The main goal of the suggested MPPT approach is to maximize the extracted PV power, or P_{PV}. After being measured and filtered by digital filters, the panel current and voltage correlative to each duty cycle, that is, each particle position are sent into the controller. The extracted power for evaluation is calculated using the fitness function based on these signals.

Step 4 (Updating individual and global optimum): The i^{th} particle's present fitness value is compared to P_{besti}, and if the current value is superior, it is updated. The global best, or G_{best}, is defined as the highest fitness value among all chosen particles.

Step 5 (Upadating position and velocity of particles): Each particle in the population has its location and velocity updated following the assessment procedure. The suggested method modifies Eq. (31) of the traditional PSO to improve tracking accuracy and speed. The inertia weight, social and cognitive coefficients are regarded as changeable factors in the APSO-based MPPT algorithm.

Eq. (31) can be revised as,

$$\emptyset_i^{k+1} = \omega^k \times \emptyset_i + c_1^k \times r_1\{P_{besti} - x_i^k\} + c_2^k \times r_2\{G_{best} - x_i^k\} \quad (32)$$

The APSO algorithm's convergence behavior is controlled by the term $\omega^k \times V^k_{i,j}$, which also instructs the particles to keep traveling in the previously investigated direction. The inertia weight is made time-varying and gradually reduced so that its impact on particle velocity diminishes as the number of iterations rises in order to improve tracking efficiency. To encourage exploration, a greater inertia weight is first provided, then it is progressively lowered over time to increase convergence speed and accuracy. To get a linear variation, the inertia weight is adjusted according to Eq. (33).

$$\omega^k = \omega_{max} - \frac{(n+\omega_{min})}{n_{max}} \quad (33)$$

where n is the current iteration index, n_1 is the total number of iterations plus one, and ω_{max} and ω_{min} are the upper and lower limits of ω^k, respectively.

Eqs. (34) and (35) describe how the values of c_1 and c_2 are changed. Both parameters are initially given relatively high values, but as iterations go on, c_1 is reduced while c_2 is raised. In particular, the particles can progressively approach the global best solution since c_1 is changed linearly in a decreasing fashion while c_2 is varied linearly in an increasing manner with time.

$$c_1^k = c_{1max} - \frac{(n+c_{1min})}{n_{max}} \quad (34)$$

$$c_2^k = c_{2max} + \frac{(n+c_{2min})}{n_{max}} \quad (35)$$

Were the upper and lower boundaries of c_1 and c_2 are represented by c_{1max}, c_{1min}, c_{2max}, and c_{2min}, respectively.

Step 6 (Looking for convergence): The convergence requirement is met and the current G_{best} value is chosen as the GMPP when the maximum number of repetitions is achieved or the velocity change falls under the designated convergence threshold.

Step 7 (Re-setting up): The PSO approach is typically used to identify the best solution for issues. When tracking solar electricity, the maximum power produced by the panel changes depending on the meteorological conditions. In order to locate fresh GMPP under changing air conditions, particles must be reinitialized. When the conditions listed in Eq. (36) is satisfied when reinitialization is carried out using the suggested method.

$$\frac{P_{PV,new} - P_{PV,last}}{P_{PV,last}} \geq \Delta P \quad (36)$$

Due to variations in environmental factors, the objective function also varies during real-time operation. In such cases, the agents should be reinitialized to track the new MPP. If reinitialization is not performed properly, P_{best} and G_{best} may not update automatically with changes in the operating point caused by environmental variations. As a result, the operating point may get trapped at a local value, preventing the search for a new MPP. To overcome this issue, an additional constraint given in Eq. (36) has been introduced.

Experimental set up and results

In order to verify the theoretical analysis and simulation results of the proposed SI-SEPIC converter, an experimental prototype has been made and tested. The circuit parameters of experimental setup are same as those used for simulation. The converter is checked under open loop condition. Figure 5 shows the experimental configuration of the suggested converter. PWM signals are generated in an open-loop arrangement using an OPAL-RT OP5600 controller with a switching frequency of f_s=50 kHz. An IRF540N MOSFET and BY229X-500 fast-recovery diodes are used in the development of the prototype. The PWM signals are amplified and electrical isolation between the control and power circuits is provided by a FOD3180 optocoupler driver integrated circuit. The FOD3180 driver is powered by a controlled 12 V DC source. The resistive load utilized to test the system is a 0–50 Ω, 5 A rheostat.

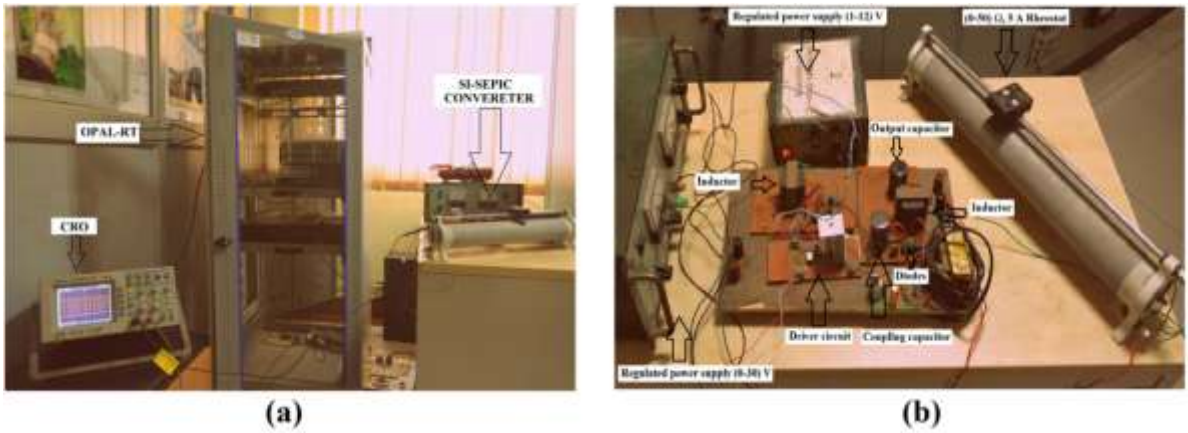


Fig. 5: Experimental setup of (a) SI-SEPIC converter, (b) SI-SEPIC converter test bench**.**

Experimental voltage and current waveforms of SI-SEPIC converter for an input of 18 V, α=0.40, Vo=24 V and Po=75 W are shown in Figure 6. Experimental waveforms of inductor L_1 and L_3 are illustrated in Figure 6(a) and Figure 6(b). It is seen that the voltage across the inductor L_1 is 18 V during ON period and 12 V during OFF period. Average value of inductor current is 2.2 A and ripple in inductor current is 1 A. Similarly, the voltage across inductor L_3 during the switch during ON period is 18 V during ON period and 12 V during OFF period. Average value of inductor current is 1.7 A, and ripple in inductor current is 0.80 A. Waveforms of diode D_1 and D_2 are shown in Figure 6(c) and Figure 6(d) respectively. The voltage across the diode D_1 is 0.7 V during ON period and it is 18 V during ON period. Alike, voltage across the diode D_2 is 12 V during ON period and 0.7 V during OFF period. Waveforms of diode D_4, and D_5 are shown in Figure 6(e) and Figure 6(f) respectively. Voltage across the diode D_4 is 18 V during ON period and it is 0.7 V during OFF period. The voltage across diode D_5 during ON period is 0 V and it is 12 V during OFF period.

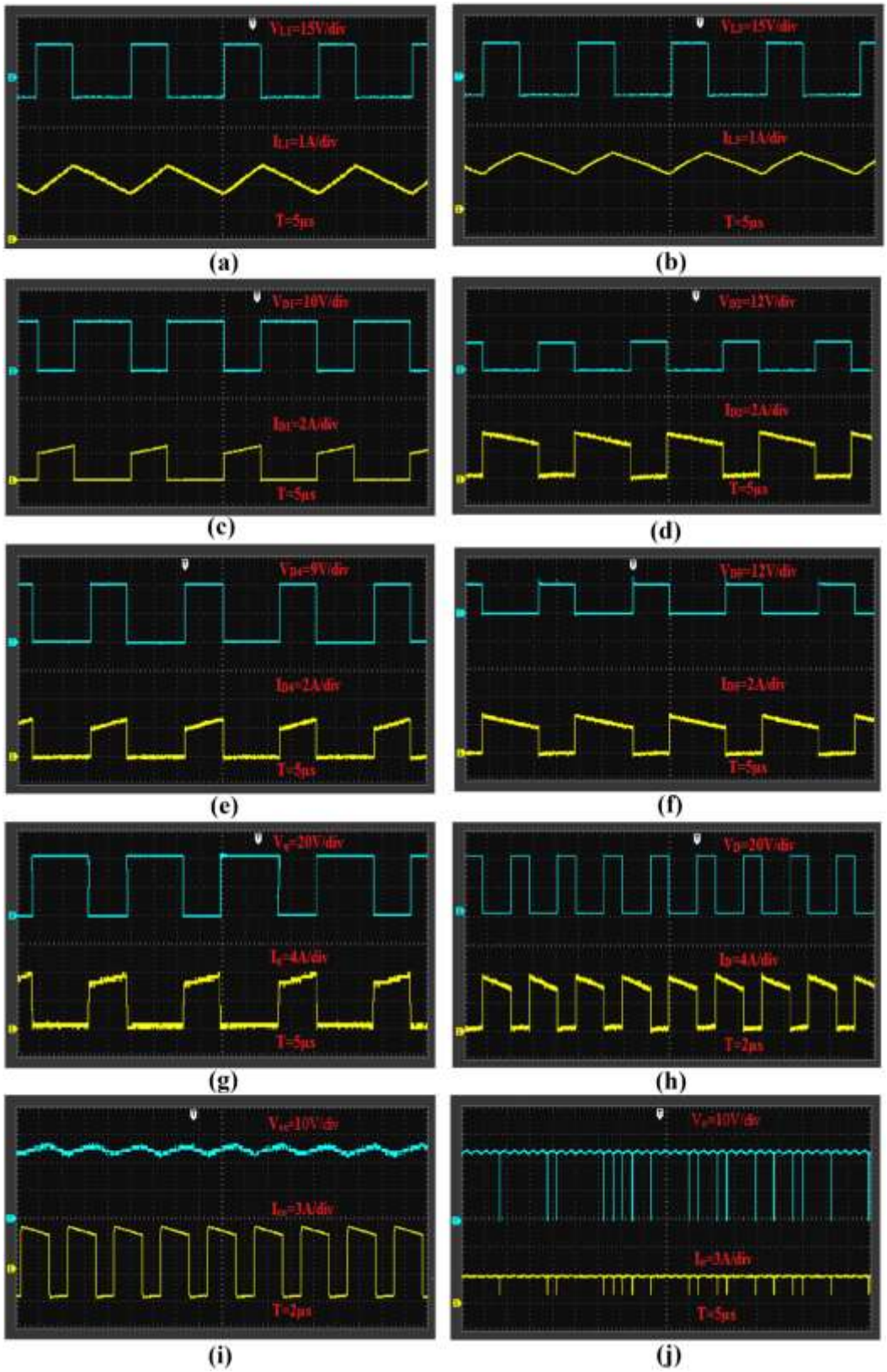


Fig. 6. Voltage and current waveforms, (a) inductor L_1, (b) inductor L_3, (c) diode D_1, (d) diode D_2, (e) diode D_4, (f) diode D_5, (g) switch Q, (f) diode D, (g) capacitor C_O and (i) load.

Waveforms across switch Q and diode D are shown in Figure 6(g) and Figure 6(h) respectively. From the results, it is observed that the voltage across the switch during ON period is 0 V and it is 42 V during OFF period. Voltage across the diode D is 42 V during ON period and it is 0.7 V during OFF period. Waveforms across capacitor Co and load are shown in Figure 6(i) and Figure 6(j) respectively. Voltage across the capacitor Co is 24 V, and ripple in voltage is 0.6 V. From the results, it is observed that the output voltage is 24 V and output current is 3.13 A.

A 75 W prototype has been developed in order to validate the suggested APSO-based MPPT approach. An OPAL-RT OP5600 controller is used in the lab to implement the APSO-based MPPT algorithm. The electricity produced by the PV panel is dissipated using a 0–50 Ω, 5 A rheostat. The suggested algorithm's performance is also confirmed and assessed using a Chroma 62150H-600S solar array simulator running in SAS mode. The efficiency of the suggested technique under various PSCs is assessed by generating distinct I–V characteristics using the "SHADOW I–V CURVE SIMULATION" function. A Hall-effect voltage and current sensors are employed to measure the input voltage and current of the SI-SEPIC converter. To measure the produced voltage and current, voltage and current sensors are attached to the PV panel's output terminals. The OPAL-RT controller receives the detected signals for MPPT operation. PWM signals produced by the controller are amplified and electrical isolation between the control and power circuits is provided by a FOD3180 driver integrated circuit. The driver circuit applies the PWM signal produced by the controller to the MOSFET switch's gate. The MATLAB/Simulink environment is used to construct the suggested APSO-based MPPT approach, which is subsequently built and downloaded into the OPAL-RT controller. Figure 7 depicts the suggested system's experimental configuration.



Fig. 7. Experimental Setup of the proposed system.

Several shade patterns were explored in order to assess the efficacy of the suggested approach under PSCs. The suggested technique was also used to analyze a shadow pattern with the

operational point situated to the right of the MPP, as seen in Figure 8. With an average power output of 42.43 W, the measured tracking efficiency is 99.89%, as shown in Figure 9.

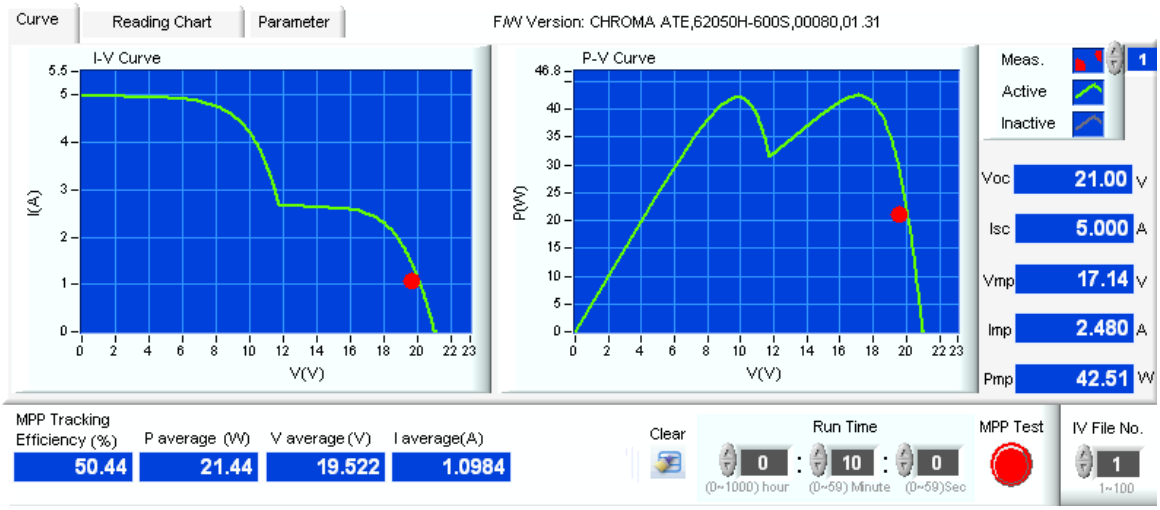


Fig. 8. Shadow pattern 1, the operating point to the MPP's right.

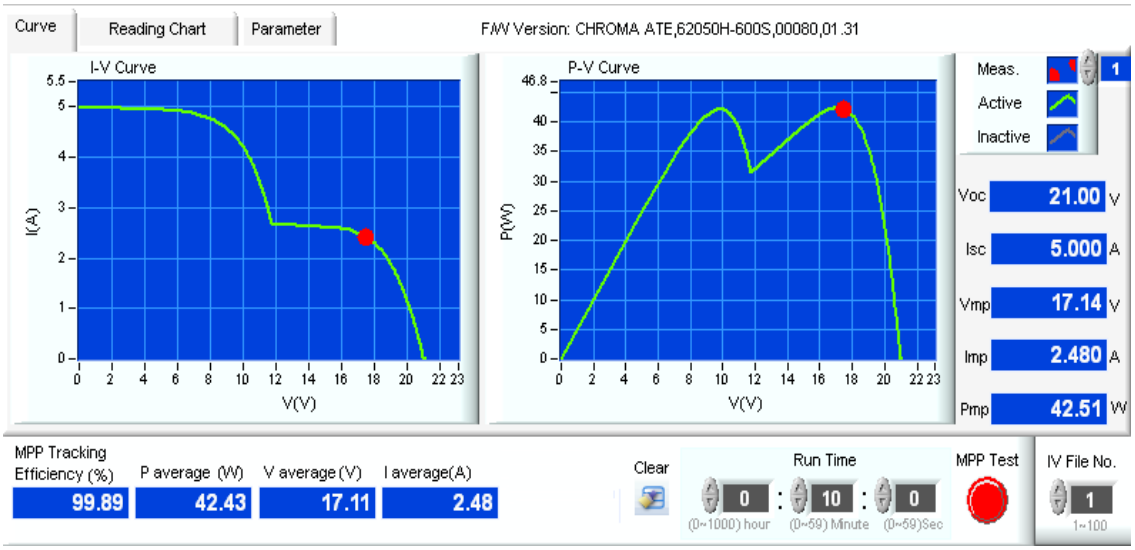


Fig. 9. Shadow pattern 1, the operating point at MPP.

The tracking procedure is then carried out when the operational point is moved to the left of the MPP, as illustrated in Figure 10. With an average output power of 42.26 W, the measured tracking efficiency is 99.89%, as shown in Figure 11.

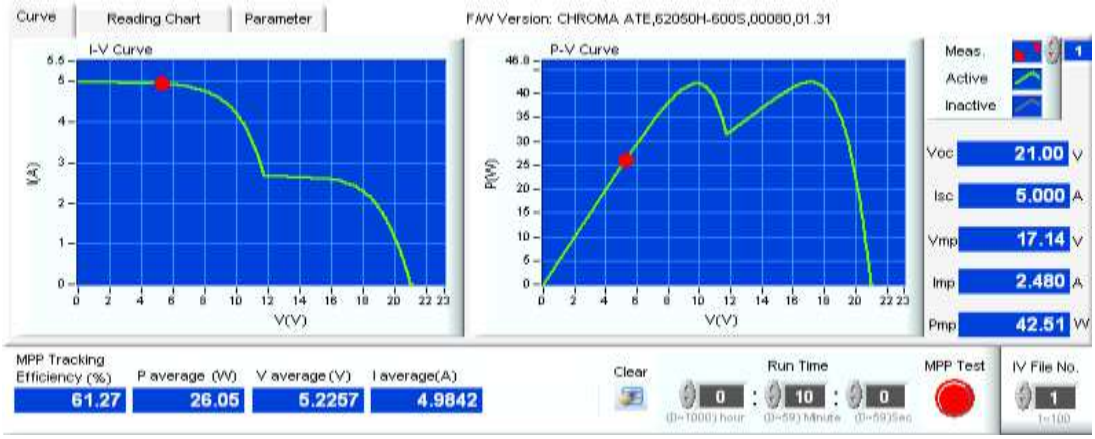


Fig. 10. Shadow Pattern 1, the operating point to the MPP's left.

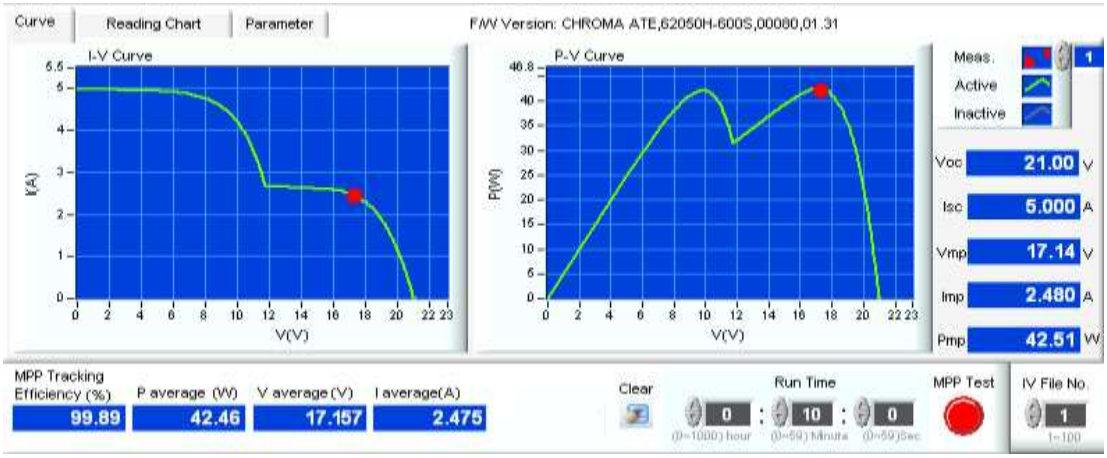


Fig. 10. Shadow Pattern 1, Operating point at MPP.

The proposed approach was also used to assess another shade pattern, as seen in Figure 11, with the operational point situated far from the MPP and to the right. With an average output power of 56.64 W, the observed tracking efficiency is 99.88%, as shown in Figure 12.

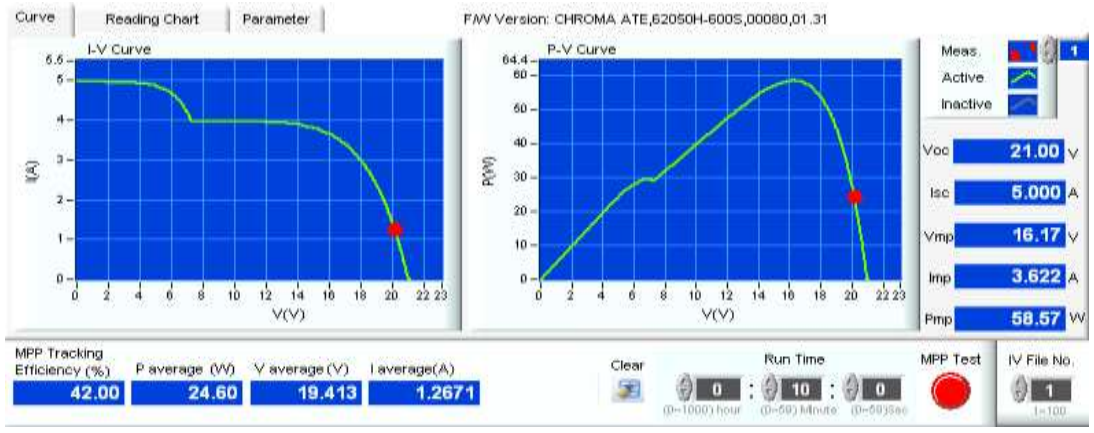


Fig. 11. Shadow pattern 2, operating point at right far away from MPP.

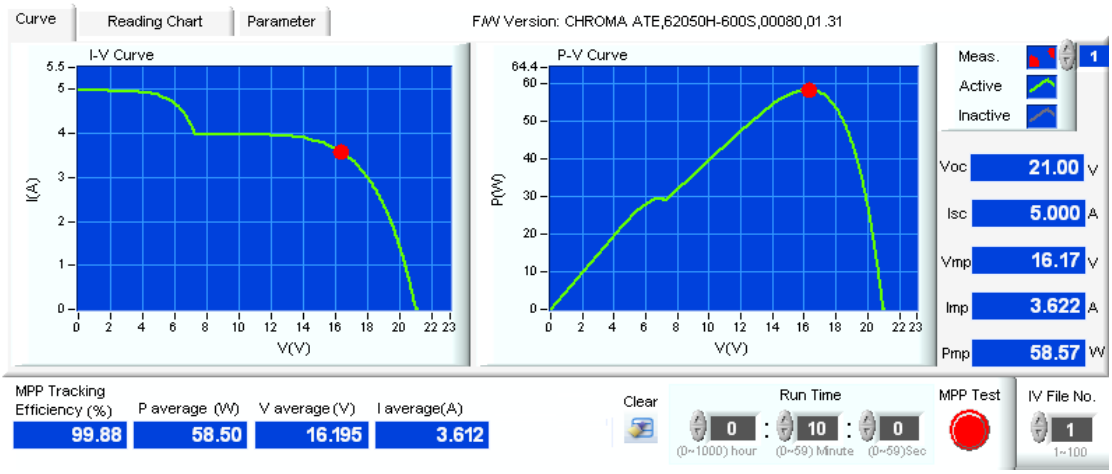


Fig. 12. Shadow pattern 2, operating point at MPP.

The tracking procedure is then completed once the operational point is moved to the left of the MPP, as seen in Figure 13. The system takes 2.30 seconds to follow the MPP, with an average output power of 56.64 W and a measured tracking efficiency of 99.80%, as depicted in Figure 14.

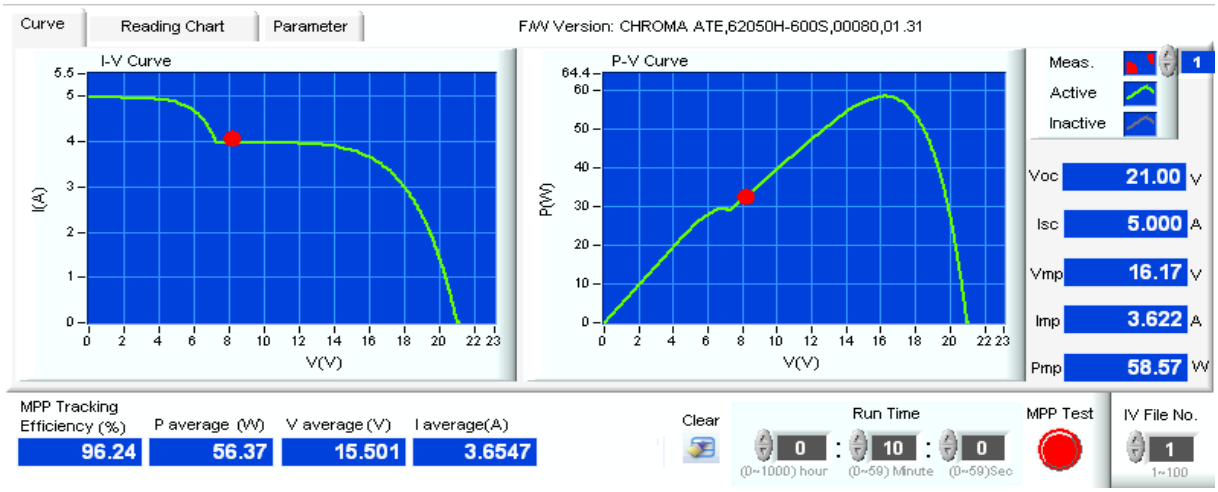


Fig. 13. Shadow pattern 2, operating point at left way from MPP.

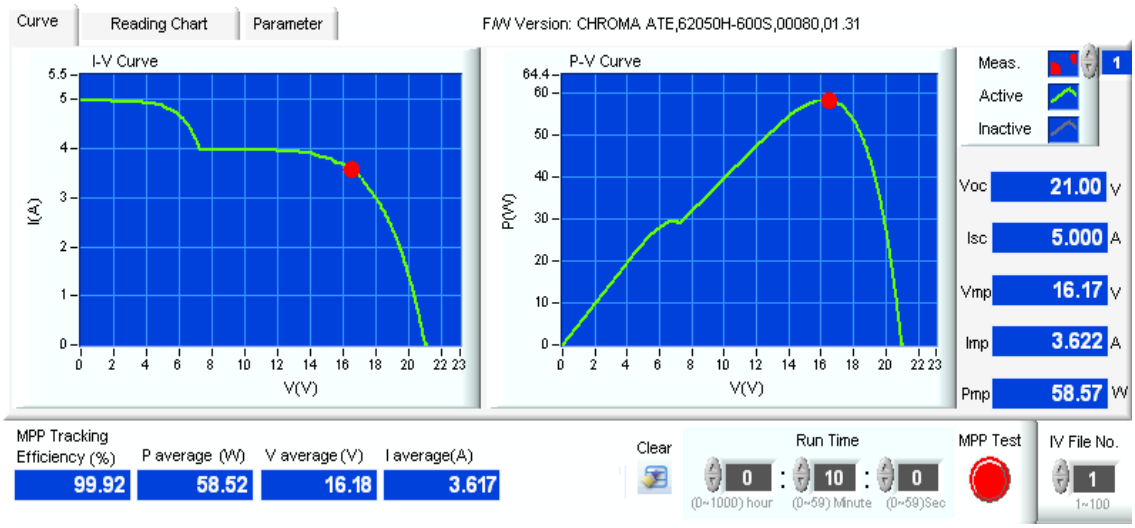


Fig. 14. Shadow pattern 2, operating point at MPP.

Conclusion

A high gain non-isolated SI-SEPIC converter is proposed for renewable energy applications in this article. The proposed converter topology aims to achieve at high voltage conversion ratio, continuous input current, voltage stress reduction across the semiconductor devices and improvement of conversion efficiency. A complete study of the converter covering the operating principles, voltage gain steady state characteristics, and design process was carried out to demonstrate its performance under practical working situations. The proposed SI-SEPIC converter is suitable for interfacing low voltage renewable energy sources with high voltage DC loads due to its significantly higher voltage gain, lower input and output current ripple and lower output voltage ripple compared to the conventional SEPIC converter. The converter retains the benefits of the typical SEPIC topology such as non-inverted output voltage and straightforward control, but provides a remarkable improvement in voltage boosting capability. The proposed converter was experimentally verified by using a laboratory prototype of 75 W. The practical results were in good agreement with the theoretical analysis and validated the stable operation, high voltage gain and efficient power conversion under diverse loading circumstances. The simple structure, high efficiency, low stress on the components and high voltage boosting capability of the proposed SI-SEPIC converter makes it very suitable for photovoltaic systems, fuel cells, battery powered systems, DC microgrids, electric vehicles, LED lighting and other high step-up renewable energy applications. Future study will include scaling up the proposed topology to larger power ratings and investigating advanced digital control approaches to further enhance dynamic performance and efficiency.

A. Funding

No funds, grants, or other support were received.

B. Authors Contributions

Dileep Gopalakrishnan: Conceptualization, methodology, formal analysis, converter design, experimentation, software, data curation, visualization, and writing—original draft. Arunkumar C R: Investigation, validation, review and editing. Vishnu Sidharthan: Investigation, validation, review and editing. Sreekanth Nethagani: Investigation, validation, review and editing. All authors reviewed and approved the final manuscript.

C. Conflicts of interest

The authors have no financial or proprietary interest in any material addressed in this paper.

D. Data availability

The data that support the findings of this study are included within the article figures and results. The data include the waveforms generated in the manuscript. During the present study no additional dataset(s) were generated or analyzed.

Reference

[1] M.E. Girgis, N.A. Elkhateeb, enhancing photovoltaic MPPT with P&O algorithm performance based on adaptive PID control using exponential forgetting recursive least squares method, Renew. Energy 237 (2024) 121801.

[2] A.H. EL-Ebiary, M.I. Marei, M. Mokhtar, Data-driven optimal adaptive MPPT techniques for grid-connected photovoltaic systems, Ain Shams Eng. J. 16 (2025) 103318.

[3] M. Mishra, P. Mahajan, R. Garg, Implementation and comparison of metaheuristically modified ANN MPPT controllers under varying solar irradiance conditions, Electr. Eng. 106 (2024) 3427–3443. [4] Toshihiko N, Shigenori T, Ryo N. Short-current pulse based adaptive maximum-power point tracking for photovoltaic power generation system IEEE and ISIE'2000, Cholula, Puebla, Mexico 2000; 157–162.

[5] Ali ANA, Saied MH, Mostafa MZ, Abdel-Moneim TM. A survey of maximum PPT techniques of PV systems. Energy Tech 2012 IEEE 2012; 1-17: 29–31.

[6] Kimball JW, Krein PT. Discrete-time ripple correlation control for maximum power point tracking. IEEE Transactions on Power Electronics 2008; 23(5): 2353–62.

[7] Kim S, Kim MBok, Youn MJ. New maximum power point tracker using sliding-mode observer for estimation of solar array current in the grid-connected photovoltaic system. IEEE Transactions on Industrial Electronics 2006; 53(4):1027–35.

[8] Coelho RF, Concer FM, Martins DC. A MPPT approach based on temperature measurements applied in PV systems. In: IEEE International Conference on Sustainable Energy Technologies 2010;1–6.

[9] Wang P, Zhu H, Shen W, Hoong CF, Chiang LP, Khoon TK. A novel approach of maximizing energy harvesting in photovoltaic systems based on bisection search theorem 2010; 2143–2148.

[10] Al Nabulsi A, Dhaouadi R. Efficiency optimization of a DSP-based standalone PV system using fuzzy logic and dual-MPPT control. IEEE Transactions on Industrial Informatics 2012;8(3):573–84.

[11] G. Perveen, P. Anand, A. Kumar, Application of ANN-ANFIS Model for forecasting solar power, Photovolt. Syst. Technol. (2024) 151–175.

[12] Y. Hakam, H. Ahessab, A. Gaga, M. Tabaa, B.E. Hadadi, Design and simulation of a 5 KW solar-powered hybrid electric vehicle charging station with a ANN–Kalman filter MPPT and MPC-based inverter control for reduced THD, Sci. Afr. 27 (2025) e02563.

[13] Z. Yan, Z. Miyuan, W. Yajun, C. Xibiao, L. Yanjun, Photovoltaic MPPT algorithm based on adaptive particle swarm optimization neural-fuzzy control, J. Intell. Fuzzy Syst. 44 (2023) 341–351.

[14] Ho BMT, Chung HSH, Lo WL. Use of system oscillation to locate the MPP of PV. IEEE Power Electronics letters 2004; 2(1).

[15] Solodovnik EV, Liu S, Dougal RA. Power controller design for maximum power tracking in solar installations. IEEE Transactions on Power Electronics 2004;19(5).

[16] Reza R, Mohammad HM, Shahriar J. Classification and comparison of maximum power point tracking techniques for photovoltaic system: A review Renewable and Sustainable Energy Reviews 2013; 19: 433-443.

[17] Salas V, Olıas E, Barrado A, Lazaro A. Review of the maximum power point tracking algorithms for stand-alone photovoltaic systems. Solar Energy Materials & Solar Cells 2006; 90: 1555-1578.
[18] Jain S, Agarwal V. Comparison of the performance of maximum power point tracking schemes applied to single-stage grid-connected photovoltaic systems. IET Electric Power Applications 2007;1(5):753–62.
[19] Hu J, Zhang J, Wu H. A novel MPPT control algorithm based on numerical calculation for PV generation systems 2009; IPEMC 2103–2107.
[20] R. Garraoui, B. Omri, M.B. Hamed, L. Sbita, A novel ANN-DISM MPPT controller for solar applications under partial shading with two-phase interleaved boost converter, Arab. J. Sci. Eng. 50 (2025) 17637–17651.
[21] M. Naiem-Ur-Rahman, M.M. Hasan, A.M. Raka, M.F. Rahman, M.M. Rana, A. A. Mansur, M.A. Razzak, An asymmetric fuzzy-based self-tuned PSO-optimized MPPT controller for grid-connected solar photovoltaic system, Energy Convers. Manag.: X 26 (2025) 100902.
[22] Tsang KM, Chan WL. Non-linear Cascade Control of DC/DC Buck Converter, Electric Power Components and Systems, ISSN: 1532-5008 (Print) 1532-5016 (Online).
[23] Vahid S, Ahmad R. A high efficiency input/output magnetically coupled interleaved buck–boost converter with low internal oscillation for fuel-cell applications: Small signal modeling and dynamic analysis Electrical Power and Energy Systems 2015: 67: 261–271.
[24] Lin B, Huang T. Zero current switching cuk converters for power factor correction, Electric power systems research 1997; 41: 91-98.
[25] I.N. Syamsiana, R.N.A. Wijaya, A.D.W. Sumari, R.N. Amalia, H. Sungkowo, Maximization of battery charging efficiency in photovoltaic systems through PI Controlled SEPIC Converter with P&O MPPT, Results Eng. 26 (2025) 105469.
[26] R.M. Esmil, A.R. Ajel, M.F. Bonnya, enhanced photovoltaic system performance through SEPIC converter optimization using hybrid ANN-PSO algorithm with MPPT strategy, AIP Conf. Proc. 3232 (2024) 050020.
[27] Chao KH. An extension theory-based maximum power tracker using a particle swarm optimization algorithm. Energy Conversion and Management 2014; 86: 435–442.
[28] A. del Rio, O. Barambones, J. Uralde, E. Artetxe, I. Calvo, Particle swarm optimization-based control for maximum power point tracking implemented in a real time photovoltaic system, Information 14 (2023) 556.
[29] S. Javed, K. Ishaque, A comprehensive analyses with new findings of different PSO variants for MPPT problem under partial shading, Ain Shams Eng. J.. 13 (2022) 101680.
[30] I. Dagal, B. Akın, E. Akboy, A novel hybrid series salp particle swarm optimization (SSPSO) for standalone battery charging applications, Ain Shams Eng. J.. 13 (2022) 101747.
[31] L. Wei, Y. Li, Research on maximum power point tracking of photovoltaic power generation based on improved hybrid optimization algorithm, Sci. Rep. 15 (2025) 3991.
[32] G. Al-Muthanna, S. Fang, I. AL-Wesabi, K. Ameur, H. Kotb, K.M. AboRas, H.Z. A. Garni, A.A. Mas'ud, A high speed MPPT control utilizing a hybrid PSO-PID controller under partially shaded photovoltaic battery chargers, Sustainability 15 (2023) 3578.
[33] L.O. Lara-Cerecedo, J.F. Hinojosa, N. Pitalúa-Díaz, Y. Matsumoto, A. Gonz´alez- Angeles, Prediction of the electricity generation of a 60-kW photovoltaic system with intelligent models ANFIS and optimized ANFIS-PSO, Energies 16 (2023) 6050.
[34] I. Dagal, B. Akın, E. Akboy, Improved salp swarm algorithm based on particle swarm optimization for maximum power point tracking of optimal photovoltaic systems, Int. J. Energy Res. 46 (2022) 8742–8759.
[35] D. Li, X. Wang, J. Wang, Z. Zhou, Differential flat & PSO based photovoltaic maximum power point tracking control under partial shading condition, Meas. Control 57 (2023) 103–112.
[36] Y. Hakam, M. Tabaa, H. Ahessab, A. Gaga, B. ELHadadi, Optimizing charging battery efficiency in partially shaded PV systems with enhanced particle swarm optimization using dual-core DSP microcontroller in EV applications, Sci. Prog. 108 (2025), https://doi.org/10.1177/00368504251334685.
[37] S. Lin, W. Liao, Research on photovoltaic dynamic MPPT algorithm based on adaptive PSO optimization, J. Comput. Methods Sci. Eng. 24 (2024) 595–609.

[38] Q.A. Ali, M.M. Elsakka, N.V. Korovkin, A. Refaat, A novel EPSO algorithm based on shifted sigmoid function parameters for maximizing the energy yield from photovoltaic arrays: an experimental investigation, Results Eng. 24 (2024) 102967.
[39] M.Z. Yousaf, M.A. Koondhar, Z.A. Zaki, E.M. Ahmed, Z.M. Alaas, I. Mahariq, J. M. Guerrero, Improved MPPT of solar PV systems under different environmental conditions utilizes a novel hybrid PSO, Renew. Energy 244 (2025) 122709.
[40] C.B. Regaya, H. Hamdi, F. Farhani, A. Marai, A. Zaafouri, A. Chaari, Real-time implementation of a novel MPPT control based on the improved PSO algorithm using an adaptive factor selection strategy for photovoltaic systems, ISA Trans. 146 (2024) 496–510.
[41] O.M.H. Anssari, M. Badamchizadeh, S. Ghaemi, Designing of a PSO-based adaptive SMC with a multilevel inverter for MPPT of PV systems under rapidly changing weather conditions, IEEE Access 12 (2024) 41421–41435.
[42] P.K. Bonthagorla, S. Yedla, A. Sakhare, S. Mikkili, A fast-adaptive coefficient particle swarm optimization MPPT technique for TT configured PV system under PSCs, Trans. Indian Natl. Acad. Eng. 10 (2025) 331–350.
[43] V. Loganathan, N.M.J. Swaroopan, MPPT of solar PV systems using PSO memetic algorithm considering the effect of change in tilt angle, Sci. Rep. 15 (2025) 7818.
[44] D. Sooriamoorthy, A. Manoharan, S.K. Sivanesan, K.L. Soon, A.C.H. Cheong, S.K. S. Perumal, Optimizing solar maximum power point tracking with adaptive PSO: a comparative analysis of inertia weight and acceleration coefficient strategies, Results Eng. 27 (2025) 106429.